

Commensurate and Incommensurate Vortex States in Superconductors with Periodic Pinning Arrays

C. Reichhardt, C. J. Olson, and Franco Nori

Department of Physics, The University of Michigan, Ann Arbor, Michigan 48109-1120

(March 25, 2021)

As a function of applied field, we find a rich variety of ordered and partially-ordered vortex lattice configurations in systems with square or triangular arrays of pinning sites. We present formulas that predict the matching fields at which commensurate vortex configurations occur and the vortex lattice orientation with respect to the pinning lattice. Our results are in excellent agreement with recent imaging experiments on square pinning arrays [K. Harada *et al.*, *Science* **274**, 1167 (1996)].

PACS numbers: 74.60.Ge

I. INTRODUCTION

The concept of an elastic lattice interacting with a rigid substrate lattice producing commensurate and incommensurate transitions when the periodicities of the two lattices match or mismatch is found in numerous condensed matter systems, including atoms adsorbed on surfaces [1], layered superconductors [2], superconducting networks and Josephson-junction arrays [3], colloids [4,5], and magnetic bubble arrays interacting with patterned substrates [6]. Recently, increased interest has been focused on superconducting systems with well defined square or triangular periodic pinning arrays in which vortices can be trapped both at individual pinning sites and also at the interstitial regions between pinning sites [7–13]. Due to the interstitial pinning, the vortex system differs significantly from systems such as atoms on surfaces or Josephson-junction arrays. For instance, in the latter systems, the potential substrate has an egg-carton form, so the atom or vortex lattice has the *same* configuration whenever it matches the underlying potential. Recent direct imaging experiments [7] and simulations [12] indicate that ordered vortex configurations in samples with periodic pinning can *vary* at each matching field, producing a remarkable variety of stabilized vortex lattices which are quite distinct from those found in superconducting networks [3] and other systems.

Since highly ordered commensurate lattices can be more strongly pinned than incommensurate lattices [7,9–12], a determination of how different matching configurations affect the overall pinning of the vortex lattice could be useful for technological applications of superconductors. For instance, enhanced pinning at certain matching fields has been verified with the observation of peaks in easily measurable magnetization curves [9,11,12], including high- T_c materials [11].

Imaging experiments have so far only probed up to the fourth matching field and have only examined square pinning arrays [7]. A general characterization of the vortex matching patterns as a function of arbitrary matching

densities for square and triangular pinning arrays has not been done up to this point.

We have performed a series of large scale simulated annealing as well as flux-gradient-driven [14] molecular dynamics simulations of vortices interacting with square and triangular arrays of small pinning sites for very high fields (up to the 28th matching field), and for a wide range of pinning parameters and system sizes.

Our results show that the vortex lattice (VL) is highly ordered only at certain matching fields (MFs) and can have various orientations with respect to the underlying pinning array. At some MFs the VL is actually disordered. The enhancements of $M(H)$ are most noticeable for fields less than the second matching field; however, we find some evidence of small enhancements of $M(H)$ for higher fields. Square and triangular arrays produce *different* sequences of ordered matching fields at which the pinning is enhanced. At some MFs, we find novel vortex arrangements with translational order only along certain directions. Our numerical results are in excellent agreement with recent low-field experiments on square pinning arrays [7]. Moreover, using geometrical arguments that take into account the constraints of the pinning array, we derive simple formulas for the ordered MFs and for the orientation of the VL with respect to the square or triangular pinning array.

II. SIMULATION

We perform simulated annealing simulations for a 2D transverse slice (in the x - y plane) of a superconducting 3D slab by numerically integrating the overdamped equation of motion of rigid 2D vortices:

$$\eta \mathbf{v}_i = \mathbf{f}_i = \mathbf{f}_i^{vv} + \mathbf{f}_i^{vp} + \mathbf{f}_i^T. \quad (1)$$

The term \mathbf{f}_i is the total force per unit length acting on vortex i . The force due to the interactions with other vortices is

$$\mathbf{f}_i^{vv} = \sum_{j=1}^{N_v} f_0 K_1 \left(\frac{|\mathbf{r}_i - \mathbf{r}_j|}{\lambda} \right) \hat{\mathbf{r}}_{ij} \quad (2)$$

where N_v is the number of vortices, $\hat{\mathbf{r}}_{ij} = (\mathbf{r}_i - \mathbf{r}_j)/|\mathbf{r}_i - \mathbf{r}_j|$, and we take $\eta = 1$. $K_1(r/\lambda)$ is the modified Bessel function, λ is the penetration depth, and

$$f_0 = \frac{\Phi_0^2}{8\pi^2\lambda^3}$$

The Bessel function decays exponentially for r greater than λ , so for computational efficiency the interaction can be safely cut off at 6λ . In thin-film superconductors the long-range vortex-vortex interaction decays as $1/r$ unlike in 3D bulk superconductors; however, the excellent agreement between our results and experiments in thin films [7] indicates that our results are valid for both slabs and thin films and are general enough to be applicable to other systems with repulsive particles on a periodic substrate (e.g., colloids). The pinning force is

$$\mathbf{f}_i^{vp} = \sum_{k=1}^{N_p} \left(\frac{f_p}{r_p} \right) |\mathbf{r}_i - \mathbf{r}_k^{(p)}| \Theta \left(\frac{r_p - |\mathbf{r}_i - \mathbf{r}_k^{(p)}|}{\lambda} \right) \hat{\mathbf{r}}_{ik}^{(p)} \quad (3)$$

where Θ is the Heaviside step function, f_p is the maximum pinning force, N_p is the number of pinning sites and $\hat{\mathbf{r}}_{ik}^{(p)} = (\mathbf{r}_i - \mathbf{r}_k^{(p)})/|\mathbf{r}_i - \mathbf{r}_k^{(p)}|$. Temperature is added as a stochastic term with properties

$$\langle f_i^T(t) \rangle = 0 \quad (4)$$

and

$$\langle f_i^T(t) f_j^T(t') \rangle = 2\eta k_B T \delta_{ij} \delta(t - t'). \quad (5)$$

To find the vortex ground state, we gradually cool a fixed number of randomly moving vortices from a high temperature to $T = 0$, simulating the field-cooled experiments of Ref. [7]. To examine vortex mobility and features in the magnetization curves as a function of applied field H , we use flux-gradient-driven simulations in which only the central 2/3 of the sample contains pinning sites. In this case, vortex lines are slowly added to the unpinned region and force their way into the pinned region (the actual sample). Although the vortex system in flux-driven simulations is in a non-equilibrium state, almost all of the vortex states found by simulated annealing also appear in the flux-driven case in parts of the sample.

We measure all lengths in units of λ and fields in Φ_0/λ^2 , and consider systems from $36\lambda \times 36\lambda$ up to $72\lambda \times 72\lambda$ in size. The pinning is placed in square or triangular arrays at densities between $n_p = 0.072/\lambda^2$ and $0.81/\lambda^2$. The pinning radius is fixed at $r_p = 0.35\lambda$. Pinning sites this size and smaller trap only *one* vortex per pinning site, which is similar to the experimental situation in Ref. [7]. We consider pinning forces f_p varying from $0.2f_0$ to f_0 and examine the VL ordering up to the 28th MF.

III. VORTEX LATTICE GROUND STATES: SQUARE CASE

A. Patterns Experimentally Observed

In Fig. 1 we show a series of VL orderings after annealing from our simulations for a square pinning array with $B = 0.17\Phi_0/\lambda^2$ for each integer MF up to the 9th MF. In (a), at the first MF, all the vortices are trapped at the pinning sites so that the overall VL is square. At the second MF (b) the interstitial vortices occupy the regions in between the pinning sites, so the overall VL is square but rotated 45° with respect to the pinning array. At the 3rd MF (c), the VL is still highly ordered, with pairs of interstitial vortices alternating in position. In (d), at the fourth MF, a VL with triangular ordering is observed. These structures for the first four MFs correspond exactly to those found in direct imaging experiments [7]. We also observe ordered VLs at the sub-MFs ($B/B_\phi = 1/4$ and $1/2$, where B_ϕ is the vortex density at the first MF), and partially ordered VLs at fractional MFs ($B/B_\phi = 3/2$ and $B/B_\phi = 5/2$) in agreement with experiment [7]. We find that the general features of the observed VL configurations up to the fourth matching field are robust for a wide range of parameters with $0.2f_0 \leq f_p \leq f_0$, and also for $0.072\Phi_0/\lambda^2 \leq B_\phi \leq 0.81\Phi_0/\lambda^2$, for system sizes up to $72\lambda \times 72\lambda$.

B. Patterns Not Yet Experimentally Observed

In Figs. 1(e-i) we show vortex configurations from our simulations that have not yet been observed experimentally. In (e), at the fifth MF, the overall VL is again square and rotated 27° with respect to the pinning lattice. In (f) a very unusual VL is observed; although the VL is neither square nor triangular some ordering is still visible. Along the $(-1, 1)$ direction the vortices are spaced periodically while in other directions apparently periodic distortions can be clearly seen. At the 7th MF, in (g), the VL is disordered. In (h), at the 8th MF, the VL is nearly triangular. In (i), at the 9th MF, a distorted square VL with two different orientations appears, separated by a twin boundary in the middle of the figure. For similar systems with lower pin density we have studied up to the 28th MF. We see the same VLs already described as well as ordered VLs at the 12th and 15th MFs, while the vortex configurations at the other MFs have no particular ordering. For $B/B_\phi > 15$, at high MFs with no overall lattice order, the VL contains ordered domains separated by grain boundaries of defects similar to those observed in Ref. [8].

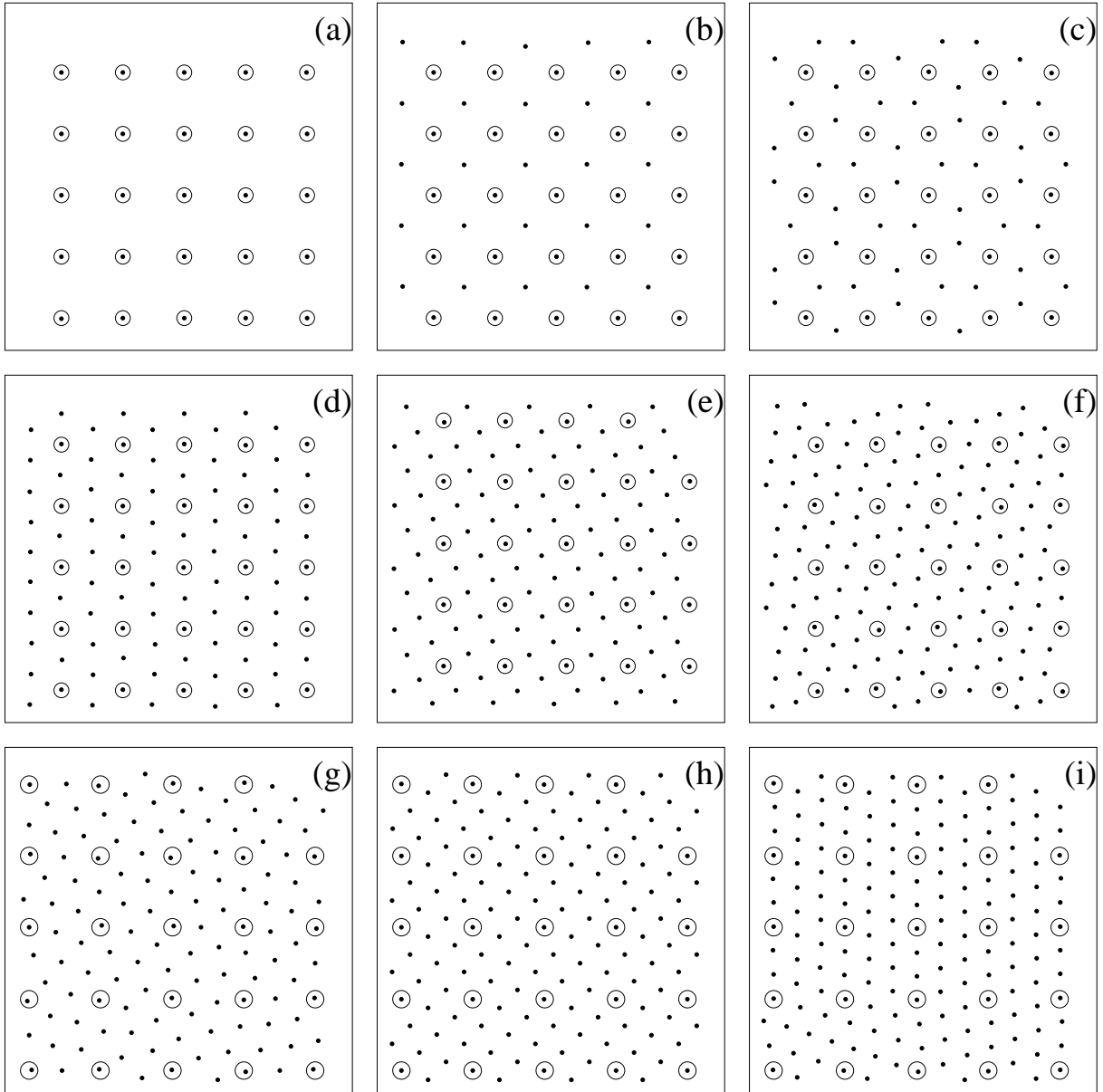


FIG. 1. Vortex ground states obtained from simulated annealing for a square pinning array with $B = 0.17 \Phi_0/\lambda^2$, $r_p = 0.35\lambda$, and $f_p/f_0 = 0.625$ showing a $12\lambda \times 12\lambda$ subset of a $36\lambda \times 36\lambda$ sample. The flux density is $B/B_\phi = 1$ in (a), 2 (b), 3 (c), 4 (d), 5 (e), 6 (f), 7 (g), 8 (h), and 9 (i).

Due to numerical constraints we could only look at pinning densities up to $n_p = 0.35\Phi_0/\lambda^2$ for $5 < B/B_\phi \leq 12$, and $n_p = 0.072\lambda^2$ for matching fields $12 < B/B_\phi \leq 28$. The vortex patterns observed here are robust for system sizes up to $72\lambda \times 72\lambda$. The fact that the same patterns appear for different-sized systems indicates that the patterns arise due to commensurability with the pinning lattice rather than commensurability with the periodic boundary conditions. We should point out that since we cannot do infinite-size systems, we cannot conclusively

rule out finite size effects on the vortex patterns observed. Also, in an experimental sample, edges and line/planar defects might distort an otherwise periodic VL and create ordered domains that do not extend over the entire sample.

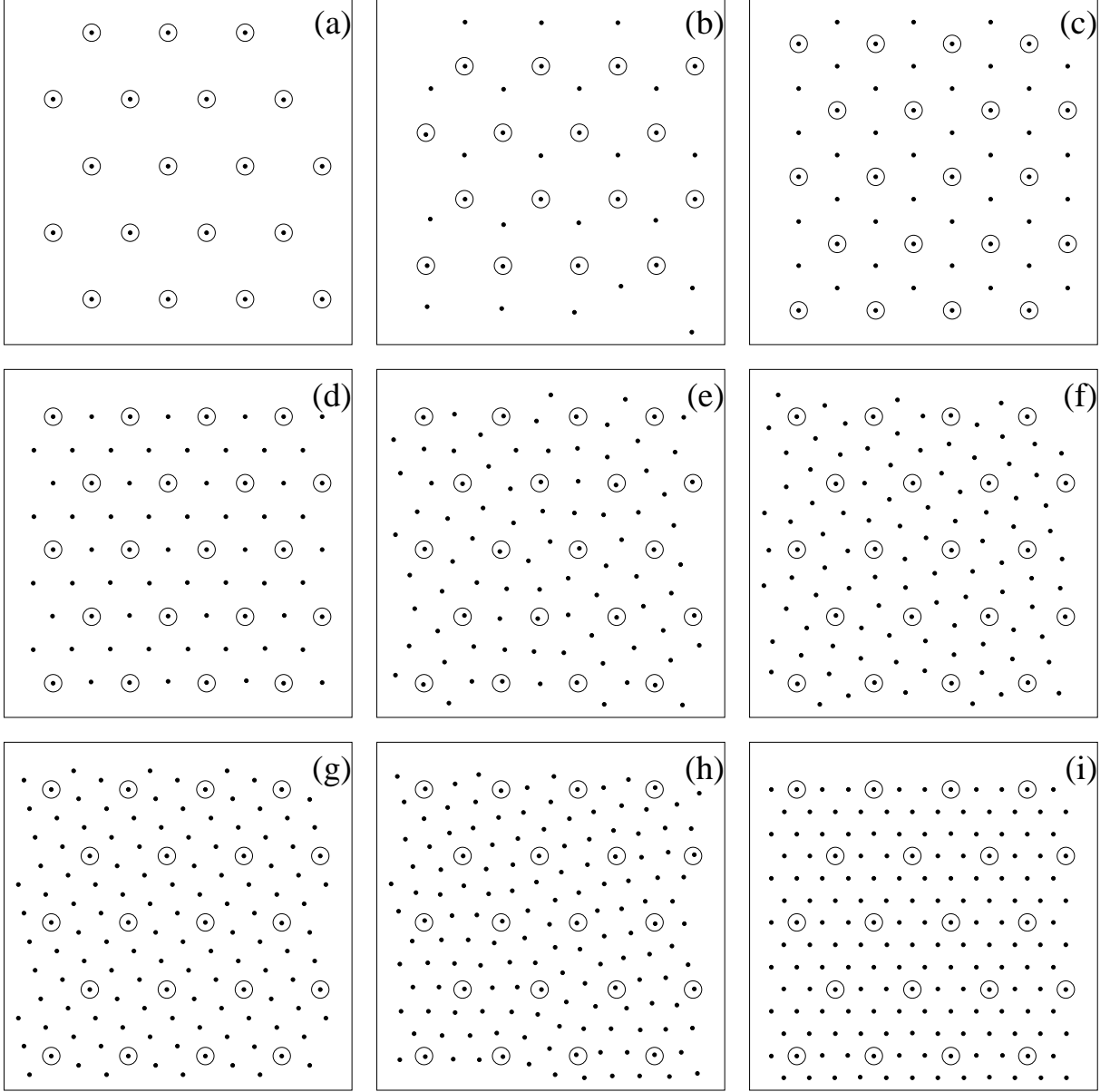


FIG. 2. Vortex ground states obtained from simulated annealing for a triangular pinning array with $B = 0.17 \Phi_0 / \lambda^2$, $r_p = 0.35\lambda$, and $f_p/f_0 = 0.625f_0$ for a $12\lambda \times 12\lambda$ subset of a $36\lambda \times 36\lambda$ sample. The flux density is $B/B_\phi = 1$ in (a), 2 (b), 3, (c), 4, (d), 5, (e), 6 (f), 7 (g), 8 (h), and 9 (i).

IV. VORTEX LATTICE GROUND STATES: TRIANGULAR CASE

In Fig. 2 we show VL configurations up to the 9th MF for a system with the same parameters as in Fig. 1 but with a triangular array of pins. In (a) at the first MF, all the vortices are pinned in a triangular lattice. In (b) a honeycomb VL forms, with some defects present. Ordered triangular VLs are seen at the 3rd (c) and 4th (d) MFs with the VL rotated 30° and 0° respectively in

relation to the pinning array. No clear ordering is seen at the 5th (e), 6th (f), and 8th (h) MFs. A triangular VL rotated 18° with respect to the pinning array is seen at the 7th (g) MF. In (i) at the 9th MF the VL is triangular and not rotated with respect to the pinning array. As in the samples with square pinning, we observe ordered VLs at certain sub-MFs but the VL is disordered at other non-MFs. The matching vortex configurations are very robust for all the parameters we have investigated, except for the honeycomb VL which disappears for weak pinning,

$f_p < 0.3f_0$. For different samples ($n_p = 0.072 \Phi_0/\lambda^2$, $f_p = 0.625f_0$) we have studied up to the 28th MF, and find ordered triangular VLs at the MFs of order 12, 13, 16, 19, 21, 25 and 28. The vortex patterns observed for the triangular pinning array are robust for a similar set of parameters as the square pinning array discussed in the previous section.

V. MATCHING CONDITIONS

To derive formulas for the fields at which VLs will be ordered, for a triangular array of pins, first take a matching field N and consider any two pinning sites along a symmetry axis that have N vortices between them. Now find a third pinning site that forms a 60° angle with the original two pinning sites, so all three vertices form an equilateral triangle. The distances between the third site and each of the other two are integer multiples of the pinning lattice constant a where

$$a = 1.075 \sqrt{\frac{\Phi_0}{B_\phi}}. \quad (6)$$

We label these integers n and m . The distance between vortices a_N at a field B is

$$a_N = 1.075 \sqrt{\frac{\Phi_0}{B}}. \quad (7)$$

By using the law of cosines the distances must obey

$$(Na_N)^2 = (ma)^2 + (na)^2 + 2mna^2 \cos(60^\circ). \quad (8)$$

At the MFs, $B = NB_\phi$, so that $a_N = a/\sqrt{N}$. Substituting this into Eq. (8) gives

$$N = m^2 + n^2 + nm. \quad (9)$$

This equality predicts that for a triangular array of pins, an ordered VL will form at values $N = 1, 3, 4, 7$, and 9, exactly as seen in our simulations in Figs. 2(a–i). Equation (9) also predicts the higher MFs ($N = 12, 13, 16, 19, 21, 25$ and 28) that we have observed numerically. The honeycomb VL seen in Fig. 2(b) is not predicted by Eq. (9) because Eq. (9) only predicts when triangular VLs occur. From Eq. (1) we find that the angle the VL makes with respect to the pinning array is

$$\theta = \arctan\left(\frac{\sqrt{3}m/2}{n + 1/2}\right). \quad (10)$$

This equation indicates that for

$$B = n^2 B_\phi, \quad (11)$$

when $m = 0$, the VL is not rotated with respect to the array of pins. This is observed for $N = 1, 4$, and 9 [shown

in Figs. 2(a), (d), and (i)], as well as for $N = 16$ and 25. For MFs $N = 3$, where $n = 1$, $m = 1$, and $N = 7$, where $n = 1$, $m = 2$, Eq. (9) gives $\theta = 30^\circ$ and 19.11° respectively, in agreement with the VLs shown in Figs. 2(c,g). We have found that Eq. (10) is valid at least up to the 28th MF studied in our simulations.

We can derive similar conditions for the square pinning array, predicting that ordered VLs appear at the N th MF when

$$N = m^2 + n^2 \quad (12)$$

This equation predicts square VLs for $N = 1, 2, 4, 5, 8$ and 9. Indeed, ordered VLs are seen at these fields (see Fig. 1). However, only $N = 1, 2$, and 5 are square in the simulation. Moreover, the angle of the VL with respect to the array of pins is in principle expected to be

$$\theta = \arctan\left(\frac{m}{n}\right) \quad (13)$$

These matching conditions do not always predict the right VL ordering observed in simulations. For instance, the VLs seen at higher fields $N > 9$ have triangular or distorted square rather than square ordering. These equations fail when the VL tendency to remain triangular dominates the tendency of the pin array to force a square ordering on the VL. This is particularly clear for higher fields, $N > 9$, when the many interstitial vortices are free to minimize their energy by forming triangular lattices. Equation (9) for the triangular array of pins does not have this limitation because *both* the sample and the VL favor a triangular order.

As we have seen from the simulations, the vortex lattice is ordered at the matching fields where the commensurability conditions outlined above are met and generally disordered where they are not. Several low matching fields where these conditions are not met still produce ordered or partially ordered lattices such as the honeycomb lattice at the second matching field for the triangular pinning lattice and the alternating interstitial lattice at the 3rd field for the square array. This ordering at fields not met by our commensurability conditions may occur due to the pinning being more dominant at lower fields so that ordering can be imposed on the interstitial vortices. For higher fields the vortex configuration for fields where commensurability conditions are not met is disordered or partially disordered. At higher fields $B > 6B_\phi$ the vortex-vortex interactions dominate. Here a triangular vortex lattice is always preferred, so any alternate ordering imposed by the pinning does not occur.

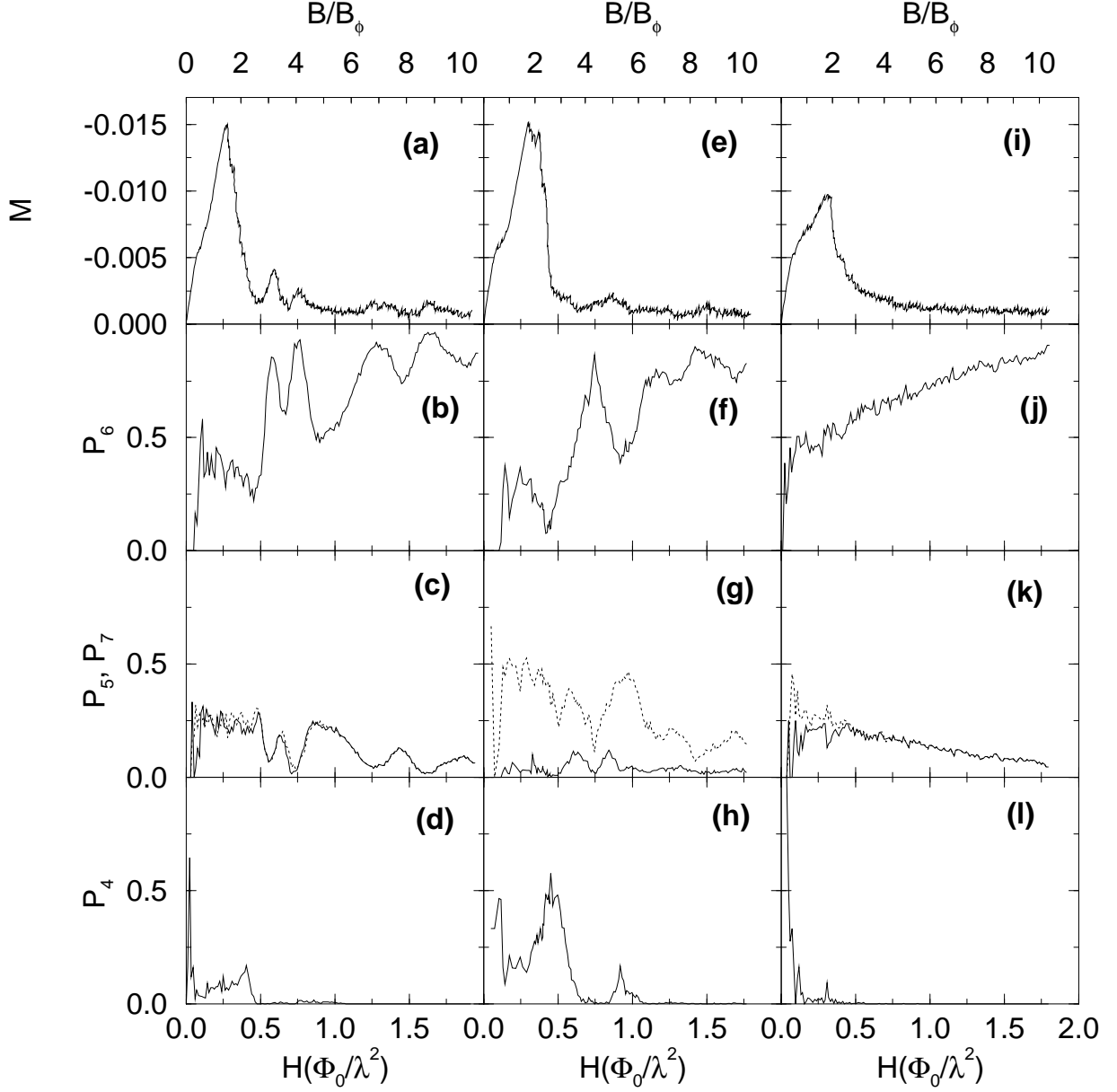


FIG. 3. Magnetization $M(H)$ and the fraction of vortices with coordination number k , $P_k(H)$, for triangular (a–d), square (e–h), and random (i–l), arrays of pins with the same pinning parameters as found in Figs. 1 and 2. In (c) and (g), P_5 (P_7) is represented with a dotted (solid) line. In (a) peaks in $M(H)$ can be seen at the 3rd, 4th, 7th and 9th MFs, which coincide with peaks in $P_6(H)$ shown in (b). For the square pinning, small peaks are seen in $M(H)$, (e), at the 2nd, 4th, 5th and 8th MFs. The 4th and 5th (small) peaks merge near the 5th MF. The peaks in P_6 , (f), indicate that the VL is triangular at the 4th, 6th and 8th MFs, while peaks in P_4 , (h), indicate that the VL is square at the 2nd and 5th MFs. Sometimes, the peak is slightly shifted (e.g. to 2.5 instead of 2 or 4.5 instead of 4) because of the gradient in the fields. In (g) P_5 is the upper curve, while in (c) and (k) P_5 and P_7 follow each other. For the random pinning array at low fields the maximum value $|M(H)|$ is $0.0095 \Phi_0/\lambda^2$, about 1.5 times less than the triangular or square pinning arrays (a,b). For $H > 0.4 \Phi_0/\lambda^2$, the magnetization $M(H)$ falls off smoothly while P_6 slowly increases as vortex-vortex interactions dominate at higher fields.

VI. TOPOLOGICAL ORDER AND MAGNETIZATION

In order to relate the MF configurations to vortex mobility as well as to experimentally measurable bulk quantities we present the magnetization $M(H)$ obtained from flux-gradient-driven simulations [12] of samples with the same pinning parameters used in Fig. 2. In Fig. 3 we plot $P_k(H)$, the fraction of vortices with coordination number k obtained from the Voronoi construction, and $M(H)$, a useful and common measurement of the net critical current. For a perfect triangular lattice $P_6 = 1$, so any departure from this indicates a defective lattice. A peak in $M(H)$ indicates enhanced pinning. In Fig. 3(a) we find that $M(H)$ is very large for fields less than about $2B_\phi$ and falls off very rapidly after this. Peaks in both $M(H)$ and $P_6(H)$ appear [Figs. 3(a,b)] at the MFs $N = 3, 4, 7$, and 9 that produced triangular VLs in the simulated annealing [Fig. (2)]. From Fig. 2(a), the vortex lattice would be expected to form a triangular lattice with the pinning substrate at the first matching field, and P_6 would be expected to be equal to one. In the flux-gradient-driven case shown in Fig. 3(a,b), no peak in $M(H)$ or P_6 near the first matching field is observed. This is due to the fact that the large *flux gradient* at low fields strongly distorts the VL. In the field cooled situation shown in Fig. 2(a) there is no gradient in the vortex density to interfere with the vortex lattice ordering. For the flux-gradient-driven case at higher fields, $B > 2B_\phi$, the gradient flattens so that the vortex lattice can become commensurate with the pinning substrate over a large area. We note that even for high matching fields a small flux-gradient will always be present so that P_6 will always be less than one as seen in Fig. 3(b). For weaker pinning, $f_p \leq 0.3f_0$, the flux gradient is reduced at low fields so that a peak in $M(H)$ and P_6 can be observed at $B/B_\phi = 1$ [12]. We find that this behavior is independent of system size. At the MFs $N = 5$ and $N = 6$ the VL is highly defective with $P_6(H)$ dropping as low as 0.5. No peak appears in $M(H)$ for the 2nd MF. For systems in which we have studied up to the 28th MF we also see some enhancements in $M(H)$ and $P_6(H)$ at the MFs predicted by Eq. (9), although the features are washed out at high fields.

In Fig. 3(e) we show $M(H)$ for a square pinning array with the same parameters used in Fig. 1. Again $M(H)$ is large for low fields and rapidly falls off after the 2nd MF. We can see a dip after the 3rd MF and an overall enhancement in $M(H)$ at the 2nd, 4th, 5th, and 8th MFs, although no clear enhancement is seen at the 6th and 9th MFs even though the VLs observed through simulated annealing at these fields also appear in this flux-gradient driven simulation. To examine the evolution of the vortices with four nearest-neighbors we consider a slightly modified Voronoi algorithm in which the lengths of each side of a Voronoi cell are compared. If the length

of any side is less than one-fourth of the average lengths of the other sides, then it is ignored. $P_4(H)$ first shows a peak at the second MF when the vortices form the lattice shown in Fig. 1(b). There is no peak in $P_4(H)$ at the first MF due to the large flux gradient. $P_6(H)$ shows a large peak at the 4th MF that corresponds to the triangular VL seen in Fig. 1(d). $P_6(H)$ then drops rapidly and $P_4(H)$ increases as the VL gains the square ordering seen in Fig. 1(e). $P_6(H)$ rises at the 6th MF and peaks at the 8th. In square pinning arrays, where we have gone up to the 28th MF, small enhancements of $M(H)$ are observed for most of the MFs that produced ordered VLs. The results indicate that, without directly imaging the VL, it could be experimentally possible to deduce the existence of the ordered vortex arrays seen here, by looking for a specific sequence of peaks in $M(H)$, at least up to the 5th matching field. Beyond the fifth matching field we observe only very small peaks in $M(H)$, which may make them difficult to see experimentally.

Our results are only valid for pins small enough that *only one* vortex can be trapped in each pinning site. With triangular pinning, peaks in $M(H)$ should in principle occur for MFs N that satisfy Eq. (9). For square pinning arrays, we observe that peaks in $M(H)$ occur for MFs given by $N = n^2 + m^2$, when $N \leq 10$, and by $N = n^2 + m^2 - 1$, when $N > 10$. This pattern of peaks differs from those already seen experimentally using periodic pinning arrays with large pinning radii, as first shown in Ref. [12]. In experiments, peaks in $M(H)$ are usually observed at every MF due to *multiple* vortices being trapped in pinning sites [9,11].

To compare the effects of random pinning to square and triangular arrays, in Fig. 3(i) we plot $M(H)$, and in Fig. 3(j-l) we plot $P_k(H)$ for a sample with the same pinning parameters as in Fig. 3(a,e) except the pinning sites are placed in a random array. It can clearly be seen that most of the peaks in P_k and $M(H)$ are washed away with $M(H)$ having a smooth falloff after the peak and the strong variations in P_k lost. The fraction of P_6 gradually increases as the vortex-vortex interactions dominate at higher fields. At the matching fields, the random array of pins has no peaks or enhancements in $M(H)$ or P_k . This suggests that the presence of peaks in the periodic pinning arrays are due to the commensurability effects with the pinning substrate.

The maximum value of the absolute value of $M(H)$, $|M(H)|$, is $0.0095 \Phi_0/\lambda^2$ for the random pinning in Fig. 3, while it is $0.015 \Phi_0/\lambda^2$ for the triangular array and square array. The latter value is about 1.5 times larger than that found for the random pinning case. This enhancement of $M(H)$ occurs only for a limited range of fields. The $M(H)$ for the triangular pinning array falls to the same value as $M(H)$ for the random pinning array at $H \approx 0.30 \Phi_0/\lambda^2$, which is less than $2B_\phi$. The $M(H)$ for the square pinning array remains higher than the $M(H)$ of the random pinning array until $H \approx 0.45 \Phi_0/\lambda^2$. This

higher value of H at which the drop occurs for the square pinning array is due to the strong commensurability at the 2nd MF for the square pinning array, whereas for the triangular array the second MF is a less stable defective honeycomb lattice. For the triangular pinning array at the third MF, $M(3B_\phi) \approx 0.004 \Phi_0/\lambda^2$, while the random pinning gives $M(3B_\phi) \approx 0.0025 \Phi_0/\lambda^2$. For fields higher than the fourth MF, $M(H)$ is of the same order for the three pinning array geometries studied here.

VII. REMARKS ON FINITE-SIZE EFFECTS

Regarding finite size effects, we would like to emphasize that we have conducted simulations in samples that vary in size from $36\lambda \times 36\lambda$ up to $72\lambda \times 72\lambda$, and we observe the same features in all our simulations regardless of the system size. We have also done simulations with different pinning strengths and observe the same peaks in $M(H)$ and $P_k(H)$. This reproducibility in the peaks in different simulations suggest that the peaks are not merely fluctuations but are robust and reproducible results. To further address this issue we have included in Fig. 3 both $M(H)$ and $P_k(H)$ for a system with the same pinning parameters as in the first two plots of $M(H)$ but with pinning placed randomly. In this plot no peaks are visible in $M(H)$ beyond the initial peak nor are any peaks visible in $P_k(H)$. The same behavior for the random array is observed for different sized systems. If the peaks in $M(H)$ in systems with square and triangular pinning are due to finite size effects such as commensurability with the boundary conditions, then peaks in $M(H)$ and P_k for system with the same size and boundary conditions but with random pinning should appear as well.

The absence of any peaks in $M(H)$ and P_k for the system with random pinning strongly suggests that peaks in these quantities for the square and triangular pinning array are due to commensurability effects with the pinning lattice only. It is important to stress that in our simulations, our analytical results and experimentally observed vortex lattice (VL) configurations are all consistent with each other.

VIII. CONCLUSION

To summarize, we have studied VLs interacting with periodic pinning arrays in which interstitial pinning is relevant above the first MF. We have shown that this system behaves considerably differently from atoms on surfaces or Josephson-junction arrays. A rich variety of distinct VLs can be stabilized including several novel partially-ordered lattices. We have also derived commensurability conditions for MFs at which stable ordered VLs appear. For the triangular pinning array these commensurability

conditions are in excellent agreement with our simulations, while for the square array the commensurability conditions work for low fields (up to the 10th matching field). Our simulations are in excellent agreement with recent imaging experiments [7] and are robust over a wide range of parameters and system sizes. Our predictions can be tested with Lorentz microscopy techniques, Bitter decoration techniques, and by looking for a specific sequence of peaks in magnetization measurements. These phases should be accessible to other systems with periodic pinning, including charged colloidal particles in a periodic array of optical traps [5], and magnetic bubble arrays interacting with patterned substrates.

IX. ACKNOWLEDGMENTS

Computer services were provided by the Maui High Performance Computing Center, sponsored in part by the Phillips Laboratory, Air Force Materiel Command, USAF, under cooperative agreement No F29601-93-2-0001. Computing services were also provided by the University of Michigan Center for Parallel Computing, partially funded by NSF Grant No CD-92-14296. C.O. acknowledges support from the NASA Graduate Student Researchers Program.

-
- [1] V.L. Pokrovsky, *Theory of Incommensurate Crystals* (Harwood, New York, 1984).
 - [2] P. Martinoli, Phys. Rev. B **17**, 1175 (1978); M. Oussena *et al.*, Phys. Rev. Lett. **72**, 3606 (1994); A. Gurevich, E. Kadyrov, and D.C. Larbalestier, *ibid.* **77**, 4078 (1996).
 - [3] L.N. Vu, M.S. Wistrom, and D.J. Van Harlingen, Appl. Phys. Lett. **63**, 1693 (1993); H.D. Hallen *et al.*, Phys. Rev. Lett. **71**, 3007 (1993); K. Runge and B. Pannetier, Europhys. Lett. **24**, 737 (1993).
 - [4] A. van Blaaderen, R. Ruel, and P. Wiltzius, Nature **385**, 321 (1997).
 - [5] D. Grier, private communication.
 - [6] J. Hu and R.M. Westervelt, Phys. Rev. B **55**, 771 (1997).
 - [7] K. Harada, O. Kamimura, H. Kasai, T. Matsuda, A. Tonomura, and V.V. Moshchalkov, Science **274**, 1167 (1996).
 - [8] T. Matsuda, K. Harada, H. Kasai, O. Kamimuram and A. Tonomura, Science **271**, 1393 (1996); F. Nori, Science **271**, 1373 (1996).
 - [9] M. Baert, V.V. Metlushko, R. Jonckheere, V.V. Moshchalkov, and Y. Bruynseraede, Europhys. Lett. **29**, 157 (1995); Phys. Rev. Lett. **74**, 3269 (1995); V.V. Moshchalkov *et al.*, Phys. Rev. B **54**, 7385 (1996); A. Bezryadin, Yu. N. Ovchinnikov, and B. Pannetier, *ibid.* **53**, 8553 (1996).

- [10] J.I. Martín, M. Vélez, J. Nogués, and I.K. Shuller, Phys. Rev. Lett. **79**, 1929 (1997).
- [11] J.Y. Lin *et al.*, Phys. Rev. B **54**, R12717 (1996); A. Castellanos *et al.*, Appl. Phys. Lett. **71**, 962 (1997).
- [12] C. Reichhardt, C.J. Olson, J. Groth, S. Field, and F. Nori, Phys. Rev. B **54**, 16108 (1996).
- [13] C. Reichhardt, C.J. Olson, and F. Nori, Phys. Rev. Lett. **78**, 1648 (1997).
- [14] Short videos are available at
<http://www-personal.engin.umich.edu/~nori>